metals

MDPI

Article

High-Entropy Alloy Laser Cladding with Cable-Type Welding Wire: Experimental Study and First-Principles Calculations

Wenjun Wang [1], Yifei Zheng [1], Zhihui Cai [2,*], Wenjian Zheng [1], Cai Zhang [2], Yu Wang [1], Zhiyong Zhao [1], Daochen Feng [1], Yinghe Ma [1] and Jianguo Yang [1]

[1] School of Mechanical Engineering, Zhejiang University of Technology, Hangzhou 310023, China; 2112102179@zjut.edu.cn (W.W.); zwj0322@zjut.edu.cn (W.Z.); 211122020151@zjut.edu.cn (Y.W.); 201906040330@zjut.edu.cn (Z.Z.)

[2] Wenzhou Special Equipment Inspection & Science Research Institute, Wenzhou 325000, China; caizhang@wzsei.com

* Correspondence: zhihui.cai@wzsei.com

Abstract: The Co-Cr-Fe-Ni high-entropy alloy (HEA) is particularly suitable for preparing coatings due to its excellent comprehensive properties. In this study, we use the laser cladding method to prepare Co-Cr-Fe-Ni HEA coatings with Co-Cr-Fe-Ni cable-type welding wire (CTWW) as the filling material and investigated the dilution rates of the coatings by experimental studies and first-principles calculations. The dilution rate is reduced to about 50% by changing the wire feeding speed, and a Co-Cr-Fe-Ni HEA coating with near nominal composition was prepared by multi-layer cladding. The HEA coating with near nominal composition is successfully prepared in the fourth layer of cladding. The coating is dense and uniform, with good metallurgical bonding. The mechanical properties of the coating were explored using first-principles calculations. All four coatings exhibit a single face-centered cubic (FCC) phase with good mechanical stability in the ground state. The bulk modulus B, shear modulus G, and Young's modulus E of the four layers of coatings are gradually decreasing from B = 202 GPa, G = 136 GPa, and E = 334 GPa to B = 239 GPa, G = 154 GPa, and E = 380 GPa. The brittleness of the coating shows a trend of first decreasing and then increasing, and the coating closest to the nominal composition has the highest brittleness.

Keywords: laser cladding; Co-Cr-Fe-Ni HEAs; cable-type welding wire; first-principles calculations; dilution

Citation: Wang, W.; Zheng, Y.; Cai, Z.; Zheng, W.; Zhang, C.; Wang, Y.; Zhao, Z.; Feng, D.; Ma, Y.; Yang, J. High-Entropy Alloy Laser Cladding with Cable-Type Welding Wire: Experimental Study and First-Principles Calculations. *Metals* **2024**, *14*, 1294. https://doi.org/10.3390/met14111294

Academic Editor: Jiro Kitagawa

Received: 23 September 2024
Revised: 30 October 2024
Accepted: 1 November 2024
Published: 16 November 2024

1. Introduction

High-entropy alloys (HEAs), as advanced materials with excellent corrosion resistance and mechanical properties that were proposed by Yeh et al. [1] and Cantor et al. [2] in 2004, have attracted widespread attention in recent years. Due to the excellent comprehensive properties of high-entropy alloys, such as outstanding impact toughness, [3] corrosion resistance, [4] wear resistance, [5] high-temperature resistance, [6] and low-temperature resistance, [7] HEAs and their coatings are widely used in fields such as the aerospace, [8] petrochemicals, [9] healthcare, [10] nuclear power, [11] and automotive industries [12]. Cui et al. [13] prepared $FeCoCrNiMnAl_x$ HEA coatings on 4Cr5MoSiV steel substrate using the laser cladding method and studied the wear resistance and oxidation resistance of $FeCoCrNiMnAl_x$ HEA coatings at high temperatures and found that the Al element promotes the transition of $FeMnCrNiCoAl_x$ coatings from face-centered cube (FCC) to FCC+ body-centered cubic (BCC) phases, effectively enhancing the high-temperature wear resistance and oxidation resistance characteristics of $FeMnCrNiCoAl_x$ coatings. Rong et al. [14] prepared FeCoNiCrX (X = Mn, Al) HEA coatings on copper substrates using the electrodeposition method and studied their microstructure, hardness, wear resistance, and corrosion resistance. They found that the HEA coating prepared exhibits a simple crystal structure in the solid solution phase and the FCC phase. The microhardness of

the coating is four times higher than that of the substrate, and the friction coefficient, wear coefficient, and wear volume are lower than those of the substrate. Moreover, in a 3.5% NaCl solution, the corrosion resistance of the HEA coating is better than that of the substrate. He et al. [15] studied the microstructure, mechanical, and corrosion resistance properties of $FeCrNiCoMnSi_{0.1}$ HEA coatings prepared by tungsten inert gas (TIG) arc melting technology and high-frequency ultrasonic impact treatment. It was found that ultrasonic impact treatment can effectively refine the microstructures of the coatings and improve their hardness, wear resistance, and corrosion resistance, especially when the ultrasonic impact power is 800 W; the performance of the coatings is optimal. Xiao et al. [16] studied the microstructures and wear behaviors of FeCoNiCrMn HEA coatings deposited on steel substrates using plasma spraying technology and investigated the effects of different hydrogen flow rates and subsequent annealing treatments on the coatings. It was found that the coating mainly presents a single-phase FCC structure, and the wear rate of the coating decreases with the increase in the hydrogen flow rate. Annealing significantly improves the wear resistance and scratch resistance characteristics of the coatings, attributed to the enhanced bonding strength of splashing in the coating and the increase in oxide content. Hsu et al. [17] prepared HEA NiCo0.6Fe0.2Cr1.5SiAlTi0.2 (C3) coating by atmospheric plasma spraying technology and evaluated its microstructure, mechanical, and oxidation resistance properties at high temperatures and found that after performing aging treatment at 800 °C and 1100 °C, the formation of the Cr3Si phase in the coating significantly improves the hardness and wear resistance. At 1100 °C, the coating exhibits excellent oxidation resistance comparable to that of typical NiCrAlY coatings due to the formation of a dense thermally grown oxide (TGO) layer composed of Al_2O_3 and Cr_2O_3. Yin et al. [18] studied the feasibility of depositing FeCoNiCrMn HEA coatings through cold spray (CS) technology and characterized its microstructure, phase composition, hardness, and wear resistance. It was found that the cold spraying process can significantly refine the grain structure of the coating, increase the hardness, and reduce the porosity and wear rate of the coating while maintaining the original phase structure of HEA. However, in these studies, although the preparation methods of HEA coatings are not the same, they all use metal powders as raw materials. It is widely acknowledged that the extensive contact surface between powder and air renders it more susceptible to oxidation. Consequently, this leads to a lower material utilization rate and higher costs associated with powders. In contrast, wire material emerges as a more favorable alternative. However, due to the lack of widespread commercial application of HEAs, the cost of preparing HEA welding wires in small batches is also very high. Shen et al. [19] proposed a method for preparing HEA welding wire in the form of multiple-stranded metal wires called cable-type welding wire (CTWW). This method uses various readily available metal wires in the market as raw materials to synthesize HEAs with the required ratio, which is cheaper and more flexible, making it possible to prepare HEA coatings by wire lasering cladding method. For example, Wang et al. [20] used CTWW to in situ synthesize carbide-reinforced Fe-Cu-Ni-Mo-Ti HEA coatings through gas tungsten arc welding (GTAW) cladding technology and found that the addition of carbon fiber enables the in situ synthesis of carbide phases in Fe-Cu-Ni-Mo-Ti-C HEA coatings, significantly improving the hardness and wear resistance of the coatings. Huang et al. [21] prepared $Nb_{37.7}Mo_{14.5}Ta_{12.6}Ni_{28.16}Cr_{7.04}$ HEA coatings using GTAW additive manufacturing technology with CTWW as filler material and investigated its microstructural and mechanical properties. The research results show that the prepared coating mainly exhibits an FCC structure and a small amount of μ phase at room temperature, with a fine and uniform dendritic structure and high hardness. The yield strength at room temperature is 545.5 MPa, and the fracture strain is 9.5%. At 750 and 1100 °C, the fracture strains are 6.5% and 6.8%, respectively, and the yield strengths are 597 and 490 MPa, respectively, which are significantly better than that of the traditional high-temperature alloy Inconel 718 (about 200 MPa at 1000 °C). Osintsev et al. [22] used CTWW arc additive manufacturing (WAAM) technology to prepare nonequiatomic $Co_{25.4}Cr_{15}Fe_{37.9}Mn_{3.5}Ni_{16.8}Si_{1.4}$ HEA (HEA) and studied its microstructure, element distri-

bution, and mechanical properties. It was found that the prepared HEA has a dendritic structure, which is mainly composed of the face-centered cubic (FCC) phase and CoCr nanoparticles with sizes of 1.5–2.5 nanometers. The element distribution is uniform and exhibits good plastic deformation behavior. The yield strength is about 279 MPa, the tensile strength is about 500 MPa, and the elongation is about 63%.

The existence of dilution behavior is undoubtedly the direct cause of changes in the compositions of HEA coatings [23–25]. Changes in composition can lead to changes in the mechanical properties of coatings. However, experimental research on coatings is easily affected by interference factors, such as experimental equipment and the environment, making it difficult to deeply study the impact of component evolution on the mechanical properties of coatings. The first-principles calculation method is based on density functional theory. As a mature calculation method, it only requires some basic physical parameters to obtain highly consistent results with experiments, and it is widely used in the study of HEAs. For example, Tong et al. [26] adjusted the compositions to improve the mechanical properties of $(NbTaW)_{1-x}Mo_x$ (x = 0, 0.05, 0.15, 0.25) alloys, especially their plasticity levels at room temperature, and found that the experimental results agreed well with the first-principles calculations. Moreover, Leong et al. [27] conducted high-throughput first-principles research on Mo-V-Nb-Ti-Zr, a refractory multi-principal element alloy (MPEA), to gain insights into the underlying microstructures. They not only illuminate the MPEA's microstructures in terms of the separation and clustering tendencies of the elements but also present a set of simple but powerful design principles for future experiments to rationally design MPEAs with the desired microstructures to enhance the mechanical properties.

In this work, we used the cable-type welding wire laser cladding (CTWW-LC) method to prepare Co-Cr-Fe-Ni HEA coatings. We also prepared Co-Cr-Fe-Ni HEA coatings, each with a composition close to the nominal composition, by multi-layer stacking with a total of four layers (L1, L2, L3, L4) fused together. Moreover, the mechanical properties of each layer of multi-layer fusion coating were studied using first-principles calculations. One novelty of this study is the use of first-principles calculations to determine the changes in the mechanical properties of HEA coatings caused by dilution rates, which helps with understanding the relationships between the dilution rates and mechanical properties of HEA coatings and provides a reference for designing and developing more excellent HEAs.

2. Experiment

2.1. Materials

The substrate used in the laser cladding process was 65 Mn spring steel, which had undergone hot rolling and stress relief annealing treatment, with dimensions of 150 mm × 100 mm × 20 mm. The chemical composition of the steel is listed in Table 1. Before cladding, the oxide skin on the surface of the substrate was polished with a hand-held grinding wheel and wiped with acetone.

Table 1. Elemental content of the base substrate material (wt.%).

Element	Fe	C	S	P	Cr	Ni	Cu	Mn
Content	Bal.	0.62~0.70	≤0.035	≤0.035	≤0.25	≤0.30	≤0.25	1.1

The Co-Cr-Fe-Ni CTWWs were prepared by a stranding wire machine, which was independently designed and produced, as shown in Figure 1. This Co-Cr-Fe-Ni CTWW was composed of four different metal wires, as shown in Figure 1b–d. The central metal wire was a high-purity Ni wire (>99.5%) with a diameter of 0.4 mm, and the surrounding six metal wires each had a diameter of 0.3 mm, of which 3 Ni-Cr wires (~50% Fe, ~25% Cr, ~25% Ni) were placed at a 120° angle. The remaining three metal wires were two high-purity cobalt wires (>99.5%) and one 304 stainless steel wire (~70% Fe, ~20% Cr, ~10% Ni). All metal wires were produced by Qinghe Runde Inc., Xingtai, China. The calculated composition of the Co-Cr-Fe-Ni CTWW is shown in Table 2.

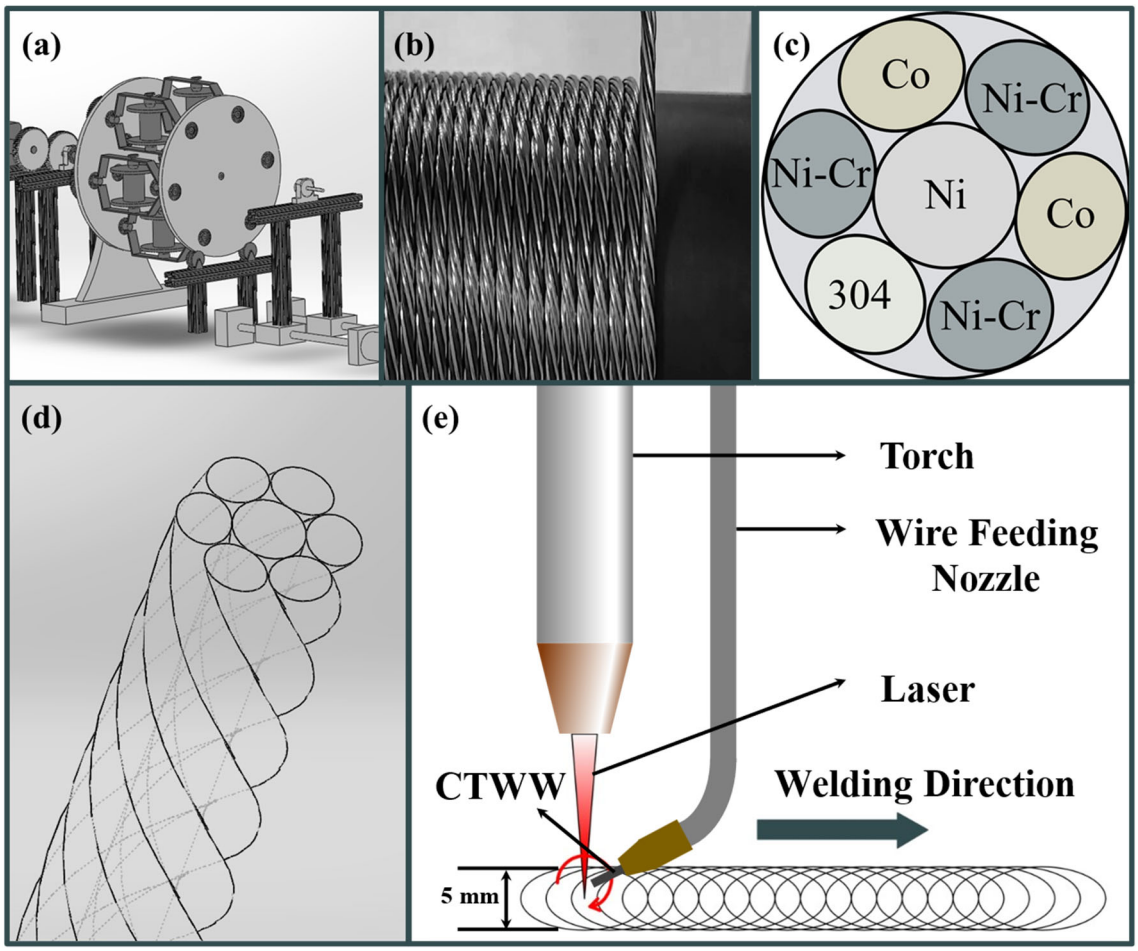

Figure 1. The laser cladding of the HEA coatings using the Co-Cr-Fe-Ni CTWWs. (**a**) The stranding wire machine. (**b**–**d**) The Co-Cr-Fe-Ni CTWWs. (**e**) The laser cladding process.

Table 2. Elemental content of the Co-Cr-Fe-Ni CTWWs (at.%).

Element	Fe	Co	Ni	Cr
Content	29.27	26.61	29.49	14.63

2.2. Laser Cladding Process

Laser cladding experiments were conducted using an HK30 laser device (0–3000 W). Then, 99.99% high-purity argon gas was used throughout the cladding process to protect the melt pool from oxidation. The specific experimental parameters were optimized through extensive testing in the early stage and, ultimately, a laser power of 2100 W, a welding speed of 4 mm/s, and a protective gas flow rate of 15 L/min. In order to obtain a larger melt pool, the laser beam was rotated and scanned to obtain a melt pool with a diameter of 5 mm. The wire feeding speed was considered a key factor affecting the dilution rate of the coating. This study aimed to obtain coatings with low dilution rates by changing the wire feeding speed, as shown in Table 3. Figure 2 shows a schematic diagram of the coating cross-section. The equation for calculating the dilution rate D was expressed as Equation (1):

$$D = \frac{h}{h + H} \quad (1)$$

where h is the molten depth of substrate (mm), and H is the thickness of the coating (mm). After selecting the optimal wire feeding speed, multi-layer cladding was performed at

that speed. The schematic diagram of the coating prepared by laser cladding is shown in Figure 1e.

Table 3. Wire feeding speed of each group.

Number	1	2	3	4	5	6	7	8	9	10
Speed (mm/s)	15	20	25	30	35	40	45	50	55	60

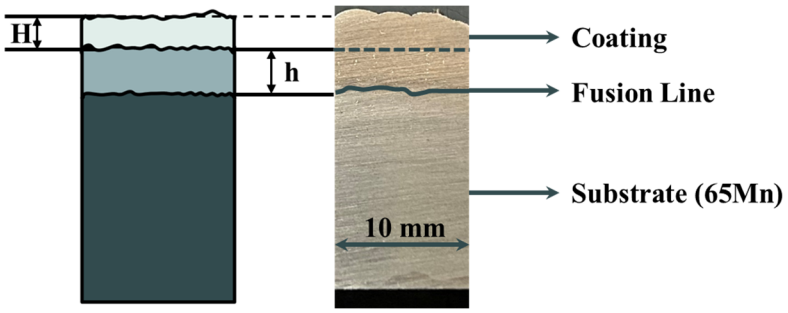

Figure 2. Fused layer cross-section diagram.

2.3. Characterization of the Coatings

An electric discharge wire-cutting machine was used to cut the coatings into small samples, and standard procedures were used to grind and polish the samples. Each sample had to be subjected to corrosion in a 4% nitric acid alcohol solution for 5 s for metallographic observation. Then, further corrosion was performed for more than 20 s for observation. The metallographic structure of each coating was observed using optical microscopy (OM, M230-USB3.0, Aosvi Inc., Shenzhen, China). The microstructure of each coating was characterized using scanning electron microscopy (SEM, Phenom XL, Phenom Inc., Shanghai, China), and the content and distribution of the alloying elements in each coating were determined using energy-dispersive X-ray spectroscopy (EDS, X-123 Fast SDD, Amptek Inc., Bedford, MA, USA). An MHVS-1000Z type digital micro-hardness tester was used to measure the micro-hardness of the coatings. The load was 200 g and the dwell time was 10 s.

2.4. First-Principles Calculations

All first principles calculations in this paper were carried out using the the Vienna ab initio simulation package (VASP 5.4.4) developed by the Hafner group at the University of Vienna based on density functional theory and the surface wave method [28]. The projector-augmented plane-wave (PAW) method [29] was used with an energy cutoff of 400 eV, and the exchange and correlation are described by Perdew–Burke–Ernzerhof (PBE) [30] in generalized gradient approximation (GGA) [31]. Simulations were performed with non-magnetic systems, a $5 \times 5 \times 5$ K-point grid, and Methfessel–Paxton smearing set to 0.2 eV. Before performing various static calculations, the conjugate gradient method was used for structural optimization, and the geometry optimizations were considered complete when the forces became smaller than 0.01 eV/Å, and the energy differences were lower than 10^{-5} eV. All the above parameters underwent convergence testing.

In this paper, the disordered single-phase HEAs solid solution structure was constructed by using the specific quasi-random structure method in ATAT software [32,33], which was developed by Axel van de Walle in collaboration with various research groups. The first-principles computational models of HEAs solid solutions in this paper were $2 \times 2 \times 2$ FCC supercellular structures and $2 \times 2 \times 2$ body-centered cubic (BCC) supercellular structures, as shown in Figure 3. All of the models contained 32 atoms. The proportions of each atom in the model were approximated relative to the actual composition. The elemental composition of each model is shown in Table 4.

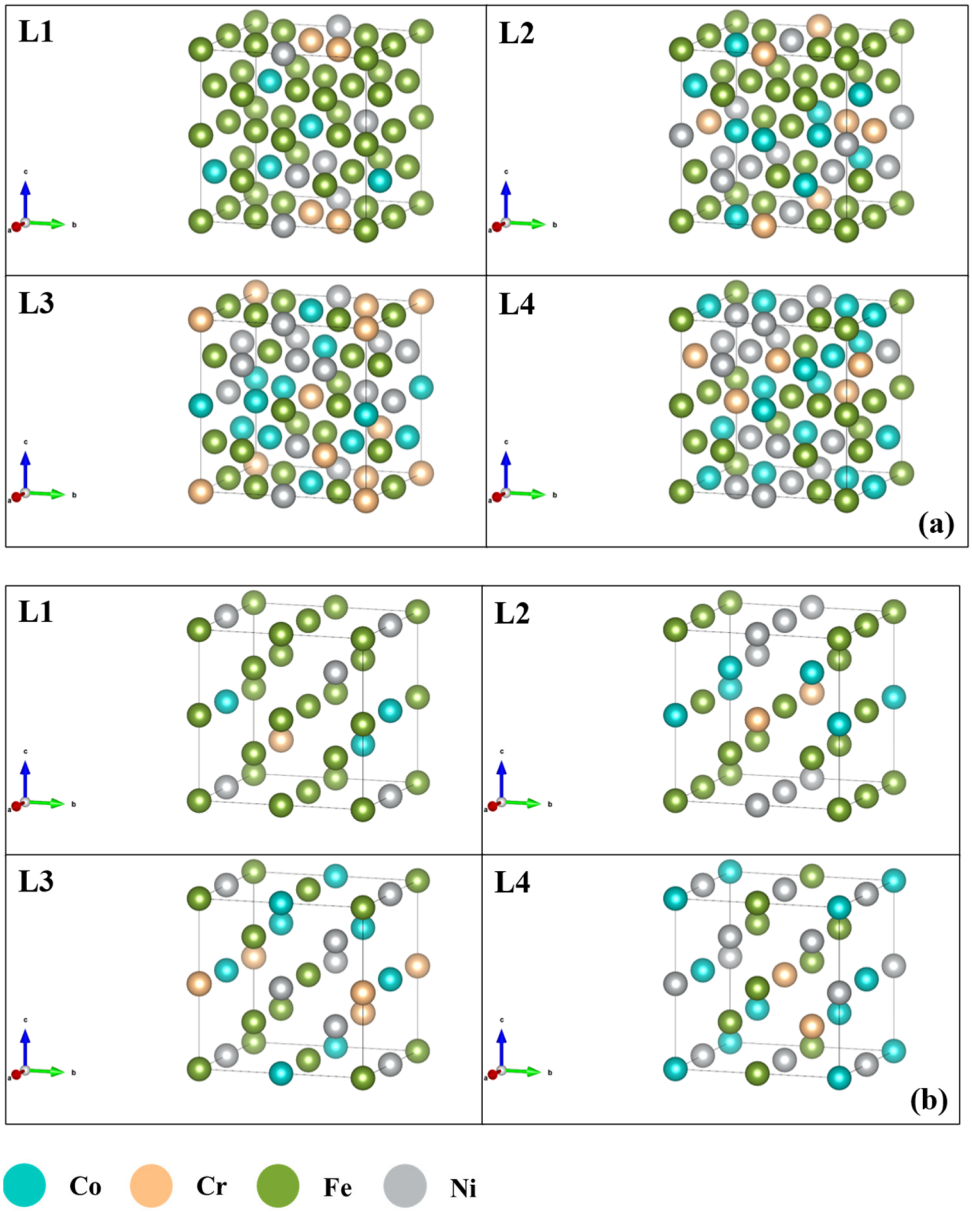

Figure 3. The unoptimized supercell models of L1, L2, L3, and L4: (**a**) FCC and (**b**) BCC.

Table 4. Atomic proportion of each model.

		Co	Cr	Fe	Ni
L1	FCC	4	2	22	4
	BCC	2	1	11	2
	At.%	12.50	6.25	68.75	12.50
L2	FCC	6	2	18	6
	BCC	3	1	9	3
	At.%	18.75	6.25	56.25	18.75
L3	FCC	8	4	12	8
	BCC	4	2	6	4
	At.%	25.00	12.50	37.50	25.00
L4	FCC	10	4	10	8
	BCC	5	2	5	4
	At.%	31.25	12.50	31.25	25.00

3. Results and Discussion

3.1. Macroscopic Morphology

The macroscopic and height diagrams of the coating are shown in Figure 4. The heights of multi-layer cladding coatings have increased from ~2 mm to ~7 mm, and the interlayer thickness is ~1.5 mm, according to Figure 4. All of the coatings have good surface qualities and no obvious surface cracks, pores, or other defects. This indicates that the CTWW-LC process adopted in this article can successfully prepare high-quality Co-Cr-Fe-Ni HEA coatings.

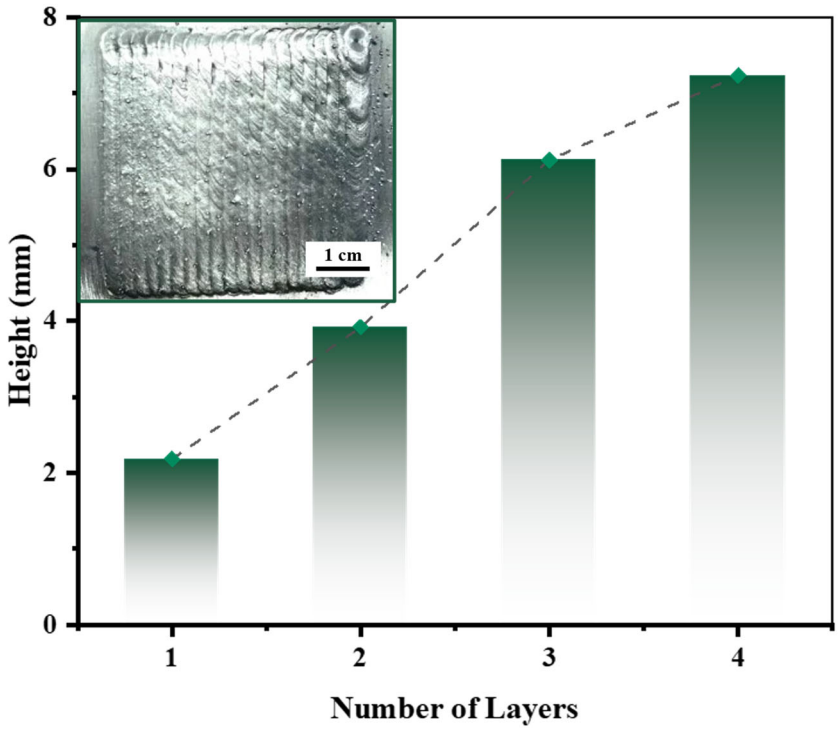

Figure 4. A macroscopic image and the heights of HEA multi-layer cladding coatings.

3.2. Influence of Dilution on the Compositions of the Coatings

According to measurement and calculation, the dilution rates of ten different coatings are shown in Table 5. The No.10 experiment was unsuccessful due to the overly fast wire feeding speed, where the welding wire was not melted and rushed out of the melt pool. The composition of each coating can be calculated by Equation (2).

$$C_x = D \times C_{BM} + (1 - D) \times C_{CTWW} \quad (2)$$

where C_x is the elemental content of the coatings, C_{BM} is the elemental content of the base substrate material, and C_{CTWW} is the elemental content of *CTWW*. The actual components obtained from EDS and the calculated components of each coating are shown in Table 6. It can be clearly seen from Tables 5 and 6 that as the wire feeding speed increases, the dilution rate decreases from over 80% to below 50%, and the composition of the coating is gradually approaching that of the *CTWW*. The calculated components are also very similar to the actual components. However, the limit of reducing the dilution rate by changing the wire feeding speed can only reach around 50%. Therefore, HEA coatings with near-nominal compositions can be obtained through multi-layer cladding. Although the dilution rate obtained with the process parameters of the No.9 experiment is the lowest, there are partially unmelted welding wires on the macroscopic surface of the sample obtained in the No.9 experiment. Therefore, the parameters of the No.8 experiment are used for multi-layer

cladding. The composition of multi-layer cladding coatings is shown in Table 7. The HEA coating with a near-nominal composition appears in L4.

Table 5. Dilution rate of each group.

Number	1	2	3	4	5	6	7	8	9	10
Dilution (%)	81.06	75.65	68.33	69.60	61.76	56.11	58.35	54.84	48.03	/

Table 6. Elemental content of each group (at.%).

Number.	Actual Composition				Calculated Composition			
	Fe	Co	Ni	Cr	Fe	Co	Ni	Cr
1	94.638	2.383	2.871	0.108	86.607	6.48	7.182	2.719
2	85.934	5.538	6.040	2.489	82.775	6.480	7.182	3.497
3	82.242	6.703	7.692	3.364	77.602	8.427	9.339	4.547
4	78.971	8.060	9.924	3.045	78.862	7.952	8.813	4.292
5	73.064	10.329	11.620	4.986	72.953	10.175	11.277	5.491
6	73.966	10.028	11.028	4.979	68.957	11.679	12.943	6.302
7	72.800	10.211	11.690	5.299	70.542	11.082	12.282	5.981
8	68.627	12.434	12.869	6.070	68.058	12.017	13.318	6.485
9	67.528	12.492	13.991	5.990	68.911	11.696	12.962	6.312

Table 7. Elemental contents of different Co-Cr-Fe-Ni HEAs layers (at.%).

		Fe	Co	Ni	Cr
Nominal composition		29.27	26.61	29.49	14.63
Actual composition	L1	68.63	12.43	12.87	6.07
	L2	54.61	17.09	19.80	9.21
	L3	37.91	23.95	26.57	11.56
	L4	33.08	26.51	28.56	11.84

3.3. Microstructure

Figure 5 shows cross-sectional metallographic images of four-layer cladding samples corroded with 4% nitric acid alcohol solution at different times in different areas. According to Figure 5a, it can be seen that there is mutual diffusion between the coating material and the substrate, forming a good metallurgical bond. At the bottom of the fusion zone, the direction of dendrite growth is opposite to the direction of heat flow and is basically perpendicular to the interface. The microstructure near the bonding line presents a small equiaxed crystal region. Figure 5d shows that the coating is uniform and free of obvious defects, such as cracks, with obvious dendritic growth, and the overall coating is a single phase. According to solidification theory [34,35], the heat of the molten pool starts to transfer outward from the center of the interface between the coating and the substrate. At this point, the temperature gradient G at the interface is high enough, and the solidification rate R is at a minimum. Therefore, the shape factor G/R tends to approach infinity, causing slow advancement of the solid–liquid interface. However, as heat transfer proceeds, the solidification rate R increases closer to the coating surface, and the cooling rate at the solidification front decreases, forming a trend of directional solidification, leading to a transition of the microstructure from small equiaxed crystal regions to columnar crystal regions. By comparing Figure 5a–d, it is clear that when the corrosion time is 5 s, the microstructure of the substrate can be clearly observed, while shallow grain boundary traces can only be observed in some areas of the coating. When the corrosion time is more than 20 s, the substrate has completely corroded and turned black, and the metallography of the coating can be clearly observed. This indicates that the corrosion resistance of the coating is much better than that of the substrate.

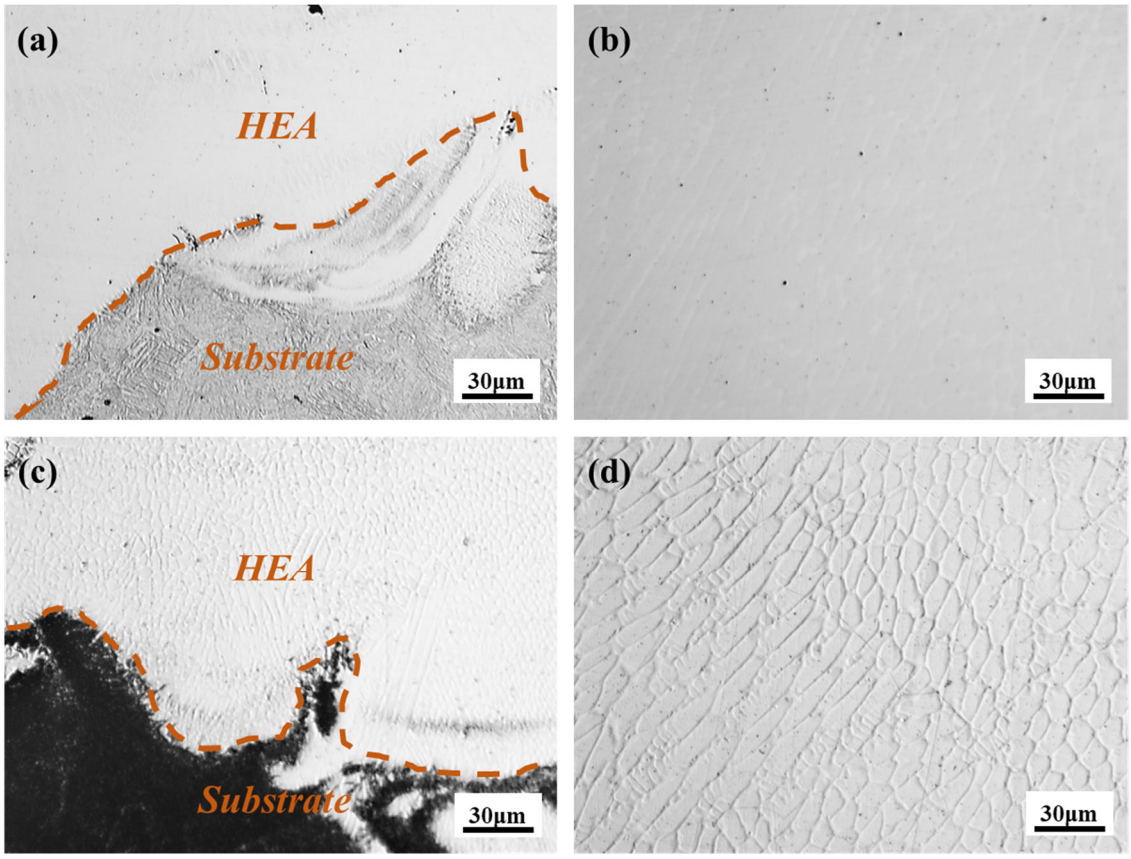

Figure 5. The cross-sectional metallographic images of four layers of cladding coating samples corroded with 4% nitric acid alcohol. (**a**) The fusion zone corroded for 5 s. (**b**) The coating corroded for 5 s. (**c**) The fusion zone corroded for more than 20 s. (**d**) The coating corroded for more than 20 s.

Figure 6a shows that the distribution of each element in the coatings is uniform without obvious segregation, which corresponds to the single-phase crystal structure. Figure 6b shows that only small amounts of Cr, Co, and Ni elements diffuse into the substrate, so it is likely that the increase in dilution rate is due to the diffusion of a large amount of iron from the substrate into the coatings.

3.4. Phase Structure

The phase structure of HEA can be predicted by empirical formulas containing atomic size difference δ and valence electron concentration VEC values. The four coatings are calculated using the following Equations (3) and (4).

The atomic size difference δ is calculated as follows:

$$\delta = \sqrt{\sum_{i=1}^{n} c_i \left(1 - \frac{r_i}{\bar{r}}\right)^2}, \ \bar{r} = \sum_{i=1}^{n} c_i r_i, \tag{3}$$

where c_i is the atomic percentage of the ith element, $\bar{r}$ is the average atomic radius of Co-Cr-Fe-Ni HEA and r_i is the atomic radius of ith element, respectively. The numerical factor 100 is used to amplify the data for clarity.

The valence electron concentration VEC is calculated as follows:

$$VEC = \sum_{i=1}^{n} c_i VCE_i, \tag{4}$$

where VEC_i is the valence electron of the ith element.

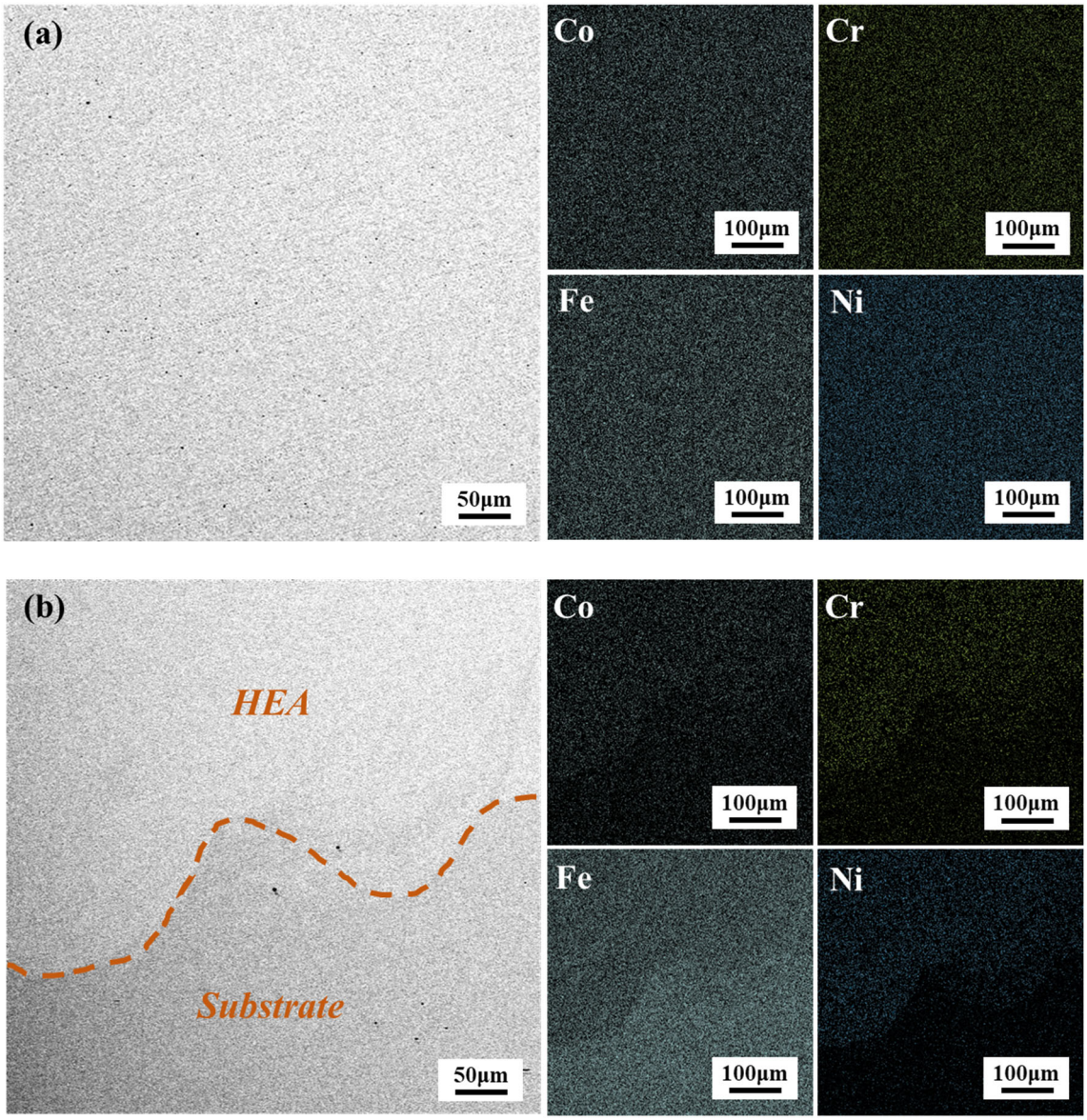

Figure 6. SEM/EDS micrographs of the HEA-based four-layer cladding coating sample: (**a**) coating and (**b**) fusion zone.

Normally, δ is considered a sign of the formation of a solid solution phase. When $\delta < 6.6\%$, the alloy is easy to form a stable disordered solid solution phase [36]. Moreover, *VEC* plays a decisive role in determining the solid solution for the FCC or BCC type of phase in HEAs. If $VEC \geq 8$, it is more likely to form an FCC phase. When $VEC < 6.87$, the BCC phase is stable. When $6.87 \leq VEC \leq 8$, the BCC and FCC structures exist simultaneously [37]. The calculation results of δ and *VEC* for the four coatings are shown in Table 8. It is obvious that L1 to L4 all conform to $\delta < 6.6$ and $VEC > 8$, so all four HEA coatings tend to form the FCC phase.

Table 8. The atomic size difference (δ) and valence electron concentration (*VEC*) values of the coatings.

Coatings	δ	*VEC*
L1	0.294	8.250
L2	0.322	8.375
L3	0.409	8.500
L4	0.315	8.594

In order to further determine the phase structure, it is also possible to predict the phase structures of HEAs from an energy perspective [38,39]. The formation enthalpy H_f and cohesive energy E_c are commonly used parameters for determining the phase structure. H_f and E_c can be calculated according to Equations (5) and (6).

$$E_c = \frac{1}{N_i}\left(E_{tot} - \sum n_i E^i_{atom}\right), \quad (5)$$

$$H_c = \frac{1}{N_i}\left(E_{tot} - \sum n_i E^i_{solid}\right), \quad (6)$$

where E_{tot} is the total energy of Co-Cr-Fe-Ni HEAs, Ni and n_i are the all-atomic numbers in supercell and every atomic number of ith constituents, respectively, E^i_{solid} is the single atom energy of a single crystal, which is completely relaxed, and E^i_{atom} is the total energy of an isolated atom in a crystal cell. In this study, the H_f and E_c values of the FCC and BCC models are calculated separately, and the results are shown in Table 9. H_f and E_c are thermodynamic indicators used to predict the formation of metal compounds and the stability of crystals. The more negative H_f and E_c are, the stronger the alloying ability of the alloy and the better the crystal stability [40]. According to Table 9, the H_f and E_c values of all FCC models are smaller than those of the BCC model. Therefore, it can be confirmed that FCC is a more stable crystal structure of Co-Cr-Fe-Ni HEA, which is consistent with previous calculation results.

Table 9. The total energy (E_{tot}) and cohesive energy (E_c) values of the coatings.

Coatings	H_f/(eV·atom^{-1})		E_c/(eV·atom^{-1})	
	FCC	BCC	FCC	BCC
L1	−0.1095	0.0312	−4.8768	−4.8497
L2	−0.1297	0.0016	−4.9601	−4.9104
L3	−0.0663	0.0427	−4.8956	4.8529
L4	−0.1163	0.2398	−4.9827	−4.6766

3.5. Influences of Different Compositions on the Mechanical Properties of the Coatings

The elastic constant is a quantity that characterizes the elasticity of a material and is used to describe the relationship between stress and strain. It is of great significance for studying the mechanical properties of alloys, such as Young's modulus and the shear modulus. The calculation of elastic constants is based on fully relaxed models, and the values are obtained through the stress–strain method. Due to the asymmetry of the supercell model, nine independent elastic constants are usually obtained. Therefore, the elastic constants are averaged using Equation (7) to reduce errors.

$$C_{11} = \frac{C'_{11} + C'_{22} + C'_{33}}{3} C_{12} = \frac{C'_{12} + C'_{23} + C'_{13}}{3} C_{44} = \frac{C'_{44} + C'_{55} + C'_{66}}{3} \quad (7)$$

The calculation results of the elastic constant are shown in Table 10. The nominal composition of L4 is close to that of CoCrFeNi HEA with an equal atomic ratio. The values of C_{11} = 317 GPa, C_{12} = 144 GPa, and C_{22} = 185 GPa for L4 are also close to the values of C_{11} = 271 GPa, C_{12} = 175 GPa, and C_{22} = 189 GPa for the CoCrFeNi HEA calculated by Tian et al. [41]. For the cubic crystal structure, mechanical stability can be determined by Equation (8) [42]:

$$C_{11} > 0,\ C_{44} > 0,\ C_{11} - C_{12} > 0,\ C_{11} + 2C_{12} > 0 \quad (8)$$

Table 10. The elastic constants of the optimized supercell model of the coatings.

	C'_{11}	C'_{12}	C'_{13}	C'_{22}	C'_{23}	C'_{33}	C'_{44}	C'_{55}	C'_{66}	C_{11}	C_{12}	C_{44}
L1	367	176	174	364	175	369	209	211	214	367	175	211
L2	351	180	179	367	184	365	194	200	203	361	181	199
L3	324	155	156	321	151	328	187	186	187	324	154	187
L4	314	146	137	321	149	317	185	184	186	317	144	185

It is obvious that all four sets of results satisfy Equation (8), which means that all four coating models have good mechanical stability in the ground state. In order to reveal the influences of component changes caused by the dilution rate on mechanical properties, the Voigt–Reus–Hill (VRH) approximation method is used to calculate the elastic modulus values of the four coatings. The results are shown in Figure 7. The bulk modulus *B* and shear modulus *G* are related to the material's ability to resist volume deformation and reversible deformation under shear stress. The larger the values of *B* and *G* are, the stronger the incompressibility and shear deformation resistance of the material. Young's modulus E characterizes the ability of crystals to resist compression or tension within the elastic range, which is closely related to the rigidity of the material. According to Figure 7, it can be seen that the bulk modulus of L1 is the highest, while the bulk modulus of L4 is the lowest, showing an overall downward trend. The shear modulus and Young's modulus also have similar trends.

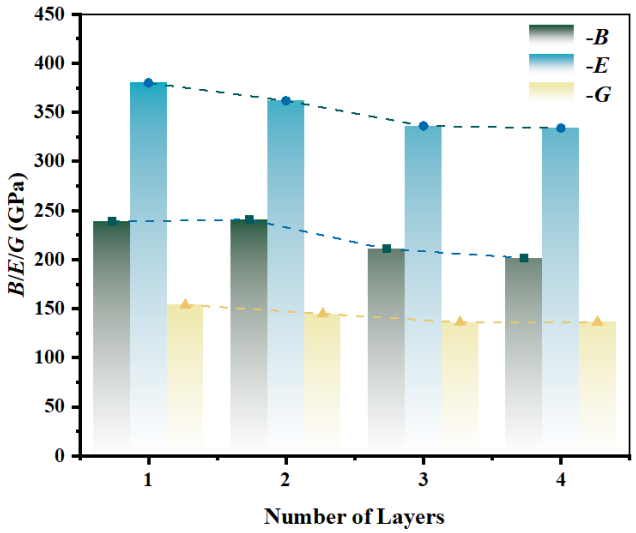

Figure 7. The moduli (*B*, *G*, and *E*) of the coatings.

The main reason for this trend is the decrease in the Fe content and the increase in the Co and Ni contents. The influences of the Fe and Ni content on the values of *B*, *G*, and *E* are completely opposite. The values of *B*, *G*, and E increase with the increase in the Fe content and decrease with the increase in the Ni content. The influence of the Co content on the value of *B* is relatively small, and it is positively correlated with the values of *G* and *E*; the Co content plays a major role in the value of *G* [43,44]. According to Table 7, it can be seen that the Fe content has decreased from 68.75% to 31.25%, and the Co and Ni contents have increased from 12.50% to 25.00% and 31.25%, respectively. Under the influences of changes in the contents of these three main elements, the overall values of *B*, *G*, and *E* show downward trends. Moreover, the Cr content is always at a lower level, so its impacts on the values of *B*, *G*, and *E* are relatively small.

The Cauchy pressure (C_{12}–C_{14}) can be used to determine the bonding mode inside materials. When C_{12}–C_{14}> 0, the material is bonded internally in the form of metal bonds. From Figure 8, it can be observed that the Cauchy pressures of all four coatings are greater

than 0, and there is no doubt that all four coatings are bonded internally with metal bonds. Toughness and brittleness are important properties of material mechanics. The toughness and brittleness of materials can be judged by the Pugh ratio (B/G) and Poisson's ratio (v). When the material simultaneously satisfies $B/G > 1.75$ and $v > 0.26$, the material exhibits good toughness characteristics. Otherwise, the material exhibits brittleness. It can be seen that the Pugh ratios of all four coatings are less than 1.75, and the Poisson's ratios are less than 0.26, according to Figure 9. Therefore, all four coatings exhibit brittle characteristics. However, this assertion contradicts the findings of Xia's [45] research. Xia's findings demonstrate that equiatomic CoCrFeNi high-entropy alloys possess superior impact toughness. This may be due to the fact that although both are alloys with the same type of element, the atomic ratios of the elements are not exactly the same, and the calculations in this study are based on the condition of 0 K, resulting in the four coatings ultimately exhibiting brittleness under the combined effects of different atomic ratios and absolute zero degrees.

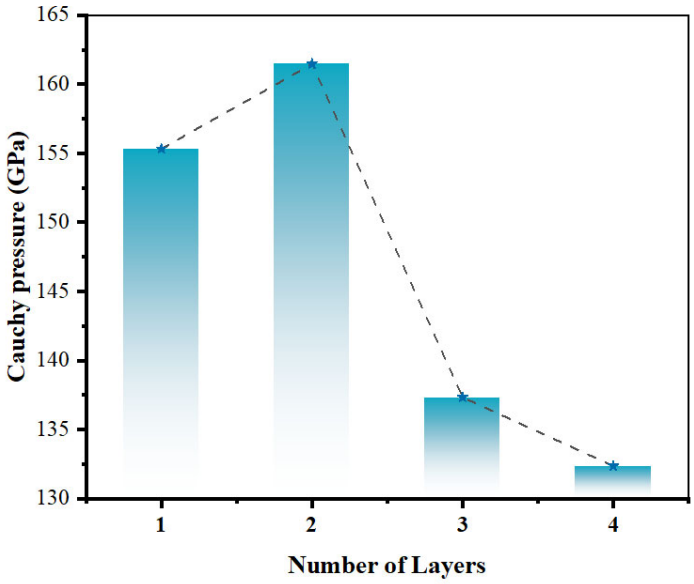

Figure 8. The Cauchy pressure (C_{12}–C_{14}) values of the coatings.

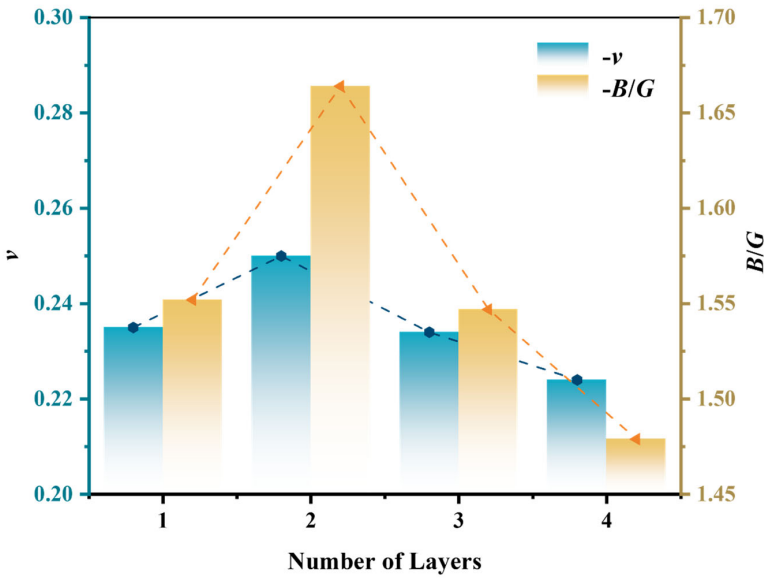

Figure 9. The Pugh ratio (B/G) and Poisson's ratio (v) values of the coatings.

4. Conclusions

In this work, the Co-Cr-Fe-Ni HEA coatings with different dilutions are developed by laser cladding technology. The chemical element distributions and microstructures of the coatings are analyzed. Furthermore, the mechanical properties of each coating are calculated using first-principles calculations. The main conclusions are as follows:

1. The dilution rate of the single-layer cladding layer can be controlled at around 50% by changing the wire feeding speed. The HEAs with near-nominal compositions can be obtained when the cladding reaches the fourth layer.
2. The CCW-LC process can achieve the manufacturing of Co-Cr-Fe-Ni HEA with a near-nominal composition that provides possibilities for the additive manufacturing of Co-Cr-Fe-Ni HEAs.
3. All four coatings exhibit a single FCC phase with good mechanical stability in the ground state.
4. The first-principles calculation results show that the bulk modulus, shear modulus, and Young's modulus values of the four layers of coatings are gradually decreasing from B = 202 GPa, G = 136 GPa, and E = 334 GPa to B = 239 GPa, G = 154 GPa, and E = 380 GPa. All four coatings satisfy $B/G < 1.75$ and $v < 0.26$, presenting brittle characteristics.

Although we have successfully prepared Co-Cr-Fe-Ni HEA coatings using the CTWW-LC method and investigated the mechanical properties of the coatings by first-principles calculations in this study, there are still some issues that need to be addressed:

1. The reduction in the dilution rate by simply changing the wire feeding speed is limited. A hot wire process can perhaps be used to reduce the input of laser energy so that only a smaller amount of substrate can be melted while the welding wire is melted. This can further reduce the dilution rate and reduce the number of layers in the multi-layer cladding.
2. The first-principles calculations of the elastic modulus are carried out at 0 K, but the reference value of the elastic modulus based on 0 K in engineering applications is not significant. Normally, the elastic moduli change is mainly controlled by volume, and the volume can change with temperature, ultimately leading to a change in the elastic modulus. Therefore, it may be possible to obtain the elastic modulus at different temperatures through relevant empirical formulas to improve the practicality of the calculation results.

Author Contributions: Conceptualization, J.Y., W.Z. and Z.C.; Methodology, W.W., Z.C. and C.Z.; Software, W.W., Y.W., Z.Z. and Z.C.; Validation, W.W. and Z.C.; Formal analysis, J.Y., W.Z., D.F. and W.W.; Investigation, Y.M., C.Z., Y.Z., Y.W. and Z.Z.; Resources, J.Y., Z.C. and W.Z.; Data curation, W.W., Y.Z., C.Z. and Y.W.; Writing-original draft preparation, W.W.; Writing-review and editing, W.Z., Y.M., D.F. and Z.C.; Visualization, W.W. and Z.Z.; Supervision, Z.C., W.Z., Y.M. and D.F.; Project administration, Z.C. and W.Z.; Funding acquisition, Z.C. and W.Z. All authors have read and agreed to the published version of the manuscript.

Funding: This work was supported by National Natural Science Foundation of China [grant number 52375391], Leading Talents Program of Zhejiang [grant number 2023C01244], and Science and Technology Plan of Market Supervision Administration of Wenzhou [grant number 2023011].

Data Availability Statement: The raw data supporting the conclusions of this article will be made available by the authors on request.

Conflicts of Interest: The authors declare that they have no conflicts of interest.

References

1. Yeh, J.W.; Chen, S.K.; Lin, S.J.; Gan, J.Y.; Chin, T.S.; Shun, T.T.; Tsau, C.H.; Chang, S.Y. Nanostructured High-Entropy Alloys with Multiple Principal Elements: Novel Alloy Design Concepts and Outcomes. *Adv. Eng. Mater.* **2004**, *6*, 299–303. [CrossRef]
2. Cantor, B.; Chang, I.T.H.; Knight, P.; Vincent, A.J.B. Microstructural development in equiatomic multicomponent alloys. *Mater. Sci. Eng. A* **2004**, *375–377*, 213–218. [CrossRef]

3. Li, D.; Zhang, Y. The ultrahigh Charpy impact toughness of forged AlxCoCrFeNi high entropy alloys at room and cryogenic temperatures. *Intermetallics* **2016**, *70*, 24–28. [CrossRef]
4. Nene, S.S.; Frank, M.; Liu, K.; Sinha, S.; Mishra, R.S.; McWilliams, B.A.; Cho, K.C. Corrosion-resistant high entropy alloy with high strength and ductility. *Scr. Mater.* **2019**, *166*, 168–172. [CrossRef]
5. Xie, H.; Tong, Y.; Bai, Y.; Li, X.; Han, Y.; Hua, K.; Wang, H. Wear-Resistance of High-Entropy Alloy Coatings and High-Entropy Alloy-Based Composite Coatings Prepared by the Laser Cladding Technology: A Review. *Adv. Eng. Mater.* **2023**, *25*, 2300426. [CrossRef]
6. Dewangan, S.K.; Mangish, A.; Kumar, S.; Sharma, A.; Ahn, B.; Kumar, V. A review on High-Temperature Applicability: A milestone for high entropy alloys. *Eng. Sci. Technol. Int. J.* **2022**, *35*, 101211. [CrossRef]
7. Lyu, Z.; Fan, X.; Lee, C.; Wang, S.-Y.; Feng, R.; Liaw, P.K. Fundamental understanding of mechanical behavior of high-entropy alloys at low temperatures: A review. *J. Mater. Res.* **2018**, *33*, 2998–3010. [CrossRef]
8. Dada, M.; Popoola, P.; Mathe, N. Recent advances of high entropy alloys for aerospace applications: A review. *World J. Eng.* **2023**, *20*, 43–74. [CrossRef]
9. Wu, H.; Wang, L.; Zhang, S.; Wu, C.L.; Zhang, C.H.; Sun, X.Y.; Chen, J. Tribological properties and sulfuric acid corrosion resistance of laser clad CoCrFeNi high entropy alloy coatings with different types of TiC reinforcement. *Tribol. Int.* **2023**, *188*, 108870. [CrossRef]
10. Liu, C.; Yang, C.; Liu, J.; Tang, Y.; Lin, Z.; Li, L.; Liang, H.; Lu, W.; Wang, L. Medical high-entropy alloy: Outstanding mechanical properties and superb biological compatibility. *Front. Bioeng. Biotechnol.* **2022**, *10*, 952536. [CrossRef]
11. Cheng, Z.; Sun, J.; Gao, X.; Wang, Y.; Cui, J.; Wang, T.; Chang, H. Irradiation effects in high-entropy alloys and their applications. *J. Alloys Compd.* **2023**, *930*, 166768. [CrossRef]
12. Kumar, A.; Gupta, M. An Insight into Evolution of Light Weight High Entropy Alloys: A Review. *Metals* **2016**, *6*, 199. [CrossRef]
13. Cui, Y.; Shen, J.; Manladan, S.M.; Geng, K.; Hu, S. Wear resistance of FeCoCrNiMnAlx high-entropy alloy coatings at high temperature. *Appl. Surf. Sci.* **2020**, *512*, 145736. [CrossRef]
14. Rong, Z.; Wang, C.; Wang, Y.; Dong, M.; You, Y.; Wang, J.; Liu, H.; Liu, J.; Wang, Y.; Zhu, Z. Microstructure and properties of FeCoNiCrX (XMn, Al) high-entropy alloy coatings. *J. Alloys Compd.* **2022**, *921*, 166061. [CrossRef]
15. He, Y.; Cong, M.; Lei, W.; Ding, Y.; Xv, T.; Han, Z. Microstructure, mechanical and corrosion properties of FeCrNiCoMnSi0.1 high-entropy alloy coating via TIG arc melting technology and high-frequency ultrasonic impact with welding. *Mater. Today Adv.* **2023**, *20*, 100443. [CrossRef]
16. Xiao, J.-K.; Tan, H.; Wu, Y.-Q.; Chen, J.; Zhang, C. Microstructure and wear behavior of FeCoNiCrMn HEA coating deposited by plasma spraying. *Surf. Coat. Technol.* **2020**, *385*, 125430. [CrossRef]
17. Hsu, W.-L.; Yang, Y.-C.; Chen, C.-Y.; Yeh, J.-W. Thermal sprayed high-entropy NiCo0.6Fe0.2Cr1.5SiAlTi0.2 coating with improved mechanical properties and oxidation resistance. *Intermetallics* **2017**, *89*, 105–110. [CrossRef]
18. Yin, S.; Li, W.; Song, B.; Yan, X.; Kuang, M.; Xu, Y.; Wen, K.; Lupoi, R. Deposition of FeCoNiCrMn HEA (HEA) coating via cold spraying. *J. Mater. Sci. Technol.* **2019**, *35*, 1003–1007. [CrossRef]
19. Shen, Q.; Kong, X.; Chen, X. Fabrication of bulk Al-Co-Cr-Fe-Ni high-entropy alloy using combined cable wire arc additive manufacturing (CCW-AAM): Microstructure and mechanical properties. *J. Mater. Sci. Technol.* **2021**, *74*, 136–142. [CrossRef]
20. Wang, Z.-Q.; Shi, Y.; Zhang, Z.-X.; Zhang, L.-J.; Wang, J.-M.; Huang, K.-H.; Chen, X.-D.; Wang, X.-R.; He, P. In situ synthesis of carbide reinforced Fe-Cu-Ni-Mo-Ti HEA coatings using GTAW cladding with cable-type welding wire. *Mater. Lett.* **2022**, *324*, 132706. [CrossRef]
21. Huang, S.; Zeng, X.; Du, X.; Peng, Z.; Li, J.; Wang, R.; Liu, J.; Yan, B.; Liu, J.; Cai, Z.; et al. Microstructure and mechanical properties of the Nb37.7Mo14.5Ta12.6Ni28.16Cr7.04 multi-principal alloys fabricated by gas tungsten wire arc welding additive manufacturing. *Vacuum* **2023**, *210*, 111900. [CrossRef]
22. Osintsev, K.A.; Konovalov, S.V.; Gromov, V.E.; Ivanov, Y.F.; Panchenko, I.A. Microstructure and mechanical properties of non-equiatomic Co25.4Cr15Fe37.9Mn3.5Ni16.8Si1.4 high-entropy alloy produced by wire-arc additive manufacturing. *Mater. Lett.* **2022**, *312*, 131675. [CrossRef]
23. Boher, C.; Younsi, T.; Soveja, A.; Chaussumier, M. Influence of iron dilution on plastic deformation mechanisms in cobalt-based alloys: Consequence of phase transformations on tribological behavior. *Wear* **2023**, *524–525*, 204845. [CrossRef]
24. Graf, K.; Tetzlaff, U.; Souza, G.B.d.; Scheid, A. Effect of dilution on the microstructure and properties of CoCrMoSi alloy coatings processed on high-carbon substrate. *Mater. Res.* **2018**, *22*, e20180502. [CrossRef]
25. Passos, T.A.; Costa, H.; Luz, F.K.; Pintaude, G. The Effect of the Dilution Level on Microstructure and Wear Resistance of Fe-Cr-CV Hardfacing Coatings Deposited by PTA-P. *Coatings* **2022**, *12*, 1835. [CrossRef]
26. Tong, Y.; Bai, L.; Liang, X.; Hua, M.; Liu, J.; Li, Y.; Zhang, J.; Hu, Y. Mechanical performance of (NbTaW)1−xMox (x = 0, 0.05, 0.15, 0.25) refractory high entropy alloys: Perspective from experiments and first principles calculations. *J. Alloys Compd.* **2021**, *873*, 159740. [CrossRef]
27. Leong, Z.; Ramamurty, U.; Tan, T.L. Microstructural and compositional design principles for Mo-V-Nb-Ti-Zr multi-principal element alloys: A high-throughput first-principles study. *Acta Mater.* **2021**, *213*, 116958. [CrossRef]
28. Kresse, G.; Hafner, J. Ab initio molecular dynamics for liquid metals. *J. Non-Cryst. Solids* **1993**, *47*, 558. [CrossRef]
29. Blochl, P.E. Projector augmented-wave method. *Phys. Rev. B Condens. Matter Mater. Phys.* **1994**, *50*, 17953–17979. [CrossRef]

30. Ernzerhof, M.; Scuseria, G.E. Assessment of the Perdew–Burke–Ernzerhof exchange-correlation functional. *J. Chem. Phys.* **1999**, *110*, 5029–5036. [CrossRef]
31. Perdew, J.P.; Burke, K.; Ernzerhof, M. Generalized Gradient Approximation Made Simple. *Phys. Rev. Lett.* **1996**, *77*, 3865–3868. [CrossRef] [PubMed]
32. van de Walle, A.; Asta, M.; Ceder, G. The alloy theoretic automated toolkit: A user guide. *Calphad* **2002**, *26*, 539–553. [CrossRef]
33. Walle, A.V.D.; Ceder, G. Automating first-principles phase diagram calculations. *J. Phase Equilibria* **2002**, *23*, 348. [CrossRef]
34. Ding, L.; Hu, S.; Quan, X.; Shen, J. Effect of VN alloy addition on the microstructure and wear resistance of Co-based alloy coatings. *J. Alloys Compd.* **2016**, *659*, 8–14. [CrossRef]
35. Song, B.; Yu, T.; Jiang, X.; Xi, W.; Lin, X. The relationship between convection mechanism and solidification structure of the iron-based molten pool in metal laser direct deposition. *Int. J. Mech. Sci.* **2020**, *165*, 105207. [CrossRef]
36. Zhang, Y.; Zhou, Y.J.; Lin, J.P.; Chen, G.L.; Liaw, P.K. Solid-Solution Phase Formation Rules for Multi-component Alloys. *Adv. Eng. Mater.* **2008**, *10*, 534–538. [CrossRef]
37. Guo, S.; Ng, C.; Lu, J.; Liu, C.T. Effect of valence electron concentration on stability of fcc or bcc phase in high entropy alloys. *J. Appl. Phys.* **2011**, *109*, 103505. [CrossRef]
38. Nong, Z.-S.; Zhu, J.-C.; Zhao, R.-D. Prediction of structure and elastic properties of AlCrFeNiTi system high entropy alloys. *Intermetallics* **2017**, *86*, 134–146. [CrossRef]
39. Hu, Y.L.; Bai, L.H.; Tong, Y.G.; Deng, D.Y.; Liang, X.B.; Zhang, J.; Li, Y.J.; Chen, Y.X. First-principle calculation investigation of NbMoTaW based refractory high entropy alloys. *J. Alloys Compd.* **2020**, *827*, 153963. [CrossRef]
40. Tong, Y.; Bai, L.; Liang, X.; Chen, Y.; Zhang, Z.; Liu, J.; Li, Y.; Hu, Y. Influence of alloying elements on mechanical and electronic properties of NbMoTaWX (X = Cr, Zr, V, Hf and Re) refractory high entropy alloys. *Intermetallics* **2020**, *126*, 106928. [CrossRef]
41. Tian, F.; Varga, L.K.; Chen, N.; Delczeg, L.; Vitos, L. Ab initio investigation of high-entropy alloys of 3d elements. *Phys. Rev. B Condens. Matter Mater. Phys.* **2013**, *87*, 075144. [CrossRef]
42. Li, Y.; Gao, Y.; Xiao, B.; Min, T.; Fan, Z.; Ma, S.; Xu, L. Theoretical study on the stability, elasticity, hardness and electronic structures of W–C binary compounds. *J. Alloys Compd.* **2010**, *502*, 28–37. [CrossRef]
43. Niu, C.; Zaddach, A.J.; Koch, C.C.; Irving, D.L. First principles exploration of near-equiatomic NiFeCrCo high entropy alloys. *J. Alloys Compd.* **2016**, *672*, 510–520. [CrossRef]
44. Liu, H.; Xin, C.; Liu, L.; Zhuang, C. Effects of Different Contents of Each Component on the Structural Stability and Mechanical Properties of Co-Cr-Fe-Ni High-Entropy Alloys. *Appl. Sci.* **2021**, *11*, 2832. [CrossRef]
45. Xia, S.Q.; Gao, M.C.; Zhang, Y. Abnormal temperature dependence of impact toughness in AlxCoCrFeNi system high entropy alloys. *Mater. Chem. Phys.* **2018**, *210*, 213–221. [CrossRef]